buildings

MDPI

Article

Numerical Simulation of Anchorage Performance of GFRP Bolt and Concrete

Gan Sun [1], Xiaoyu Bai [1], Songkui Sang [1], Ling Zeng [2], Jichao Yin [1], Desheng Jing [3], Mingyi Zhang [1] and Nan Yan [1,*]

[1] School of Civil Engineering, Qingdao University of Technology, Qingdao 266520, China
[2] School of Civil Engineering, Changsha University of Science & Technology, Changsha 410114, China
[3] Nanjing Metro Town Development and Construction Group Co., Ltd., Nanjing 210000, China
* Correspondence: yannan0527@163.com

Abstract: We conducted anchoring performance, stress distribution, and full-scale indoor pulling tests on glass-fiber-reinforced polymer (GFRP) bolts. The tests were conducted using finite element software while considering the multi-interface contact and BK criterion by using the cohesive element to simulate the contact relations between the anchor rod body and concrete and building an axial symmetry calculation model of the GRFP bolt and concrete. The results indicated that the finite element model based on cohesive element accurately represents the load–displacement relationship of the GFRP bolt and the distribution law of axial stress along the anchoring length. In addition, the simulation outcomes of the load–displacement relationship were in good agreement with the measured test values. Under the same load, the axial-force-transferred depth of the bolt body was identical regardless of the anchorage length. As anchoring length increases, the pull load on the bolt and the decay rate of axial stress along the anchoring length rises gradually. There is a critical value for the anchorage length of the bolt.

Keywords: laboratory test; anchorage length; critical anchoring length; bond stress

check for updates

Citation: Sun, G.; Bai, X.; Sang, S.; Zeng, L.; Yin, J.; Jing, D.; Zhang, M.; Yan, N. Numerical Simulation of Anchorage Performance of GFRP Bolt and Concrete. *Buildings* **2023**, *13*, 493. https://doi.org/10.3390/buildings13020493

Academic Editor: Ahmed Senouci

Received: 14 January 2023
Revised: 27 January 2023
Accepted: 2 February 2023
Published: 11 February 2023

1. Introduction

Due to the increasing prevalence of underground buildings, the buried depth of building foundations is gradually increasing, and anti-floating structure treatment is imperative. Due to its simple construction, safety, effectiveness, and low cost, the anti-floating anchor has been widely used [1,2]. As a permanent support, anti-float bolts are affected in the long term by salt ions in groundwater, and their durability becomes more of a problem [3–5]. The GFRP bolt can fundamentally solve the durability problem of the anti-floating bolt due to its material and mechanical properties. Because of the differences in material properties, the anchoring mechanism of the GFRP bolt varies from that of traditional reinforcement [6–8], where anchoring refers to the interaction between the GFRP anchor and concrete, and the length of the GFRP anchor in concrete is called the anchoring length.

Utilizing experiment, theory, and numerical simulation, scholars have explored the interaction mechanism between GFRP anchor and concrete, especially the bond between GFRP anchor and concrete. In this field, experimental studies are critical. Laboratory tests have the advantages of providing good controllability, high efficiency, and low costs, making them the primary method for researchers to examine the bond performance of GFRP bolts. Soong et al. [9], using an indoor pull-out test, determined that the strength of the interface between the GFRP anchor and concrete was primarily borne by chemical bonding, while bearing resistance and frictional resistance play a minor role. Kou et al. [10] embedded an FBG sensor into the GFRP anchor to monitor the stress variation of the GFRP anchor during the pulling process. They indicated that there was a critical depth in the GFRP anchor system, and when the length of the bolt exceeded the critical value, the tensile capacity of the bolt did not change significantly. Lu et al. [11] yielded identical results through experiments. As the bond length of the GFRP bolt increased, the ultimate pulling load of the bolt rose [12], the slip amount of the bolt gradually decreased [13,14], and the average bond strength between the bolt and concrete dropped [15,16]. When the bonding length exceeded a specific value, the failure mode of the bolt changed from pulling-out failure to concrete-splitting failure [17]. The end-bearing effect produced by additional ribs can effectively reduce the cracking of the concrete; a moderate increase in the number of additional ribs can maximize the tensile strength of FRP bars and improve the bond strength between FRP bars and concrete [18–20]. Additionally, the concrete strength [21–23], the covering thickness of the concrete [24], and the environmental conditions [25,26] also impact the bonding strength of the GFRP bolt to concrete.

Geotechnical engineering poses great difficulties because of its high concealment, highly complex research elements, and high field-test cost. Numerical analysis software, which is under continuous development, has become the primary research tool in many fields. Based on the bond-slip law of the GFRP bolt derived from laboratory tests, Gooranorimi et al. [27] used ABAQUS software to develop a parametric bond-slip model for the GFRP bolt and discovered that the thickness of concrete affects the bonding strength of the bolt. Yoo et al. [28] proposed equations for the normalized bond strength and development length of GFRP rebar embedded in UHPFRC, with pull-out failure relying on the test results. Tekle et al. [17,29] used the constitutive bond-slip method to conduct finite element simulation and indicated that the distribution of bond stress of the GFRP bolt is not uniform, with the degree of bonding stress nonuniformity depending on the bonding length of the bolt. Rezazadeh et al. [30] built a finite element model to simulate the bonding behavior of the GFRP bolt and demonstrated that the thickness of the concrete overlay impacts the bonding strength of the bolt when the nonlinearity of concrete and GFRP bar-concrete interface is considered.

Few studies have been conducted on applying computer analysis methods to anti-floating engineering, and the GFRP anchor bolt model is rough, which seriously influences the test findings. This study conducted numerical simulation research on the anchoring mechanism of GFRP anti-float bolts and concrete using ABAQUS finite element software. The feasibility of the concrete anchorage model was verified by comparing the simulation and test results. In addition, this model was employed to analyze the anchoring mechanism between a GFRP bolt and concrete with different anchoring lengths and to investigate the influence of anchoring length on anchoring performance, thereby providing a theoretical foundation for the design of GFRP anti-float bolts.

2. ABAQUS Simulation Boundary Relationships

2.1. ABAQUS Software

ABAQUS is a finite element analysis software that can solve simple linear and complex nonlinear problems, and it is commonly applied in construction engineering. ABAQUS/CAE is an ABAQUS modeling module with a simple operation interface and strong flow. The ABAQUS software provides directly extractable geotechnical constitutive models, including the typical Mole-Coulomb, D-P, modified Cambridge, concrete damage models, and others. The interaction module offers a variety of interface parameter settings that can solve the contact relationship between different components. The load module can assign values to boundary conditions and model loads. These advantages make ABAQUS finite element analysis well-suited to handling a wide variety of engineering challenges.

In conclusion, ABAQUS finite element software can be utilized to simulate the GFRP bolt pulling test and model the anchorage between the GFRP bolt and concrete. The cohesive interface relationship and concrete damage constitutive models based on ABAQUS can be applied to model GFRP anchor concrete, simulating the pull test of the GFRP anchor. The GFRP anchor and concrete were simulated using a four-node bilinear axisymmetric quadrilateral element of CAX4R. The boundary conditions are set according to the actual situation of the anti-floating anchor. The model is validated by field or laboratory tests. This demonstrates the feasibility of using ABAQUS for FRP anchor analysis.

2.2. Realization Method of the Interface Bonding Relation

The interface bonding between the GFRP bolt and concrete is the key to numerical simulation. There is chemical bonding, bearing resistance, and frictional resistance between the GFRP bolt and the concrete interface [9]. This study used a cohesive model to define this interfacial relationship. Generally, this model can realistically simulate the interfacial friction between bolt and concrete. The model also simplifies the complex interfacial failure process to a correlation between the relative displacement and force between the two separated interfaces. The cohesive model can be implemented by either creating contact units or setting up contact relations.

2.2.1. Contact Units

In this study, the cohesive model was introduced by creating contact units. The procedure started by setting up a single layer of cohesive elements where cracks and relative displacement were expected to be generated between various components. Thereafter, the bond displacement characteristics were represented in this unit. The cohesive unit can be part of a component, creating a cohesive layer using component cutting zones. Moreover, the cohesive unit can be a single solid component with binding constraints on other components. These two modeling approaches, shown in Figure 1, can model the layered failure of composite materials, but the former method is complicated in grid division, and the latter is complicated in assembly and contact relation settings. Accordingly, the suitable method can be selected based on structure shape, material, and other differences.

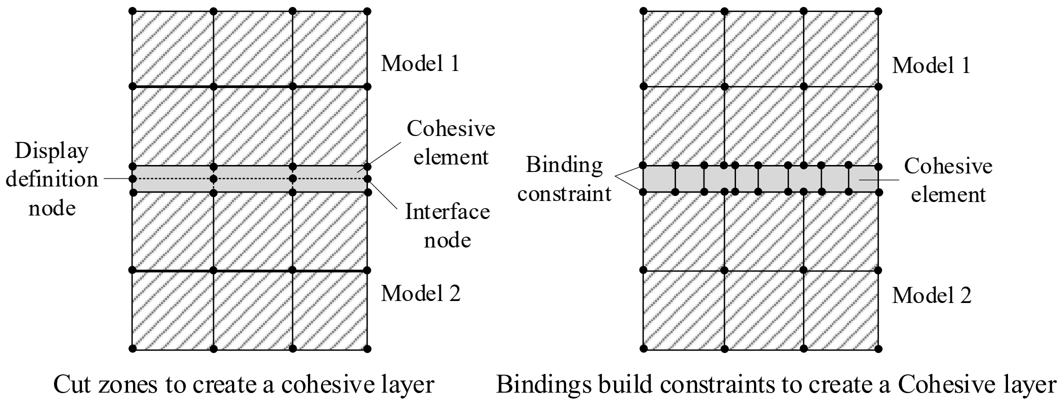

Figure 1. Schematic diagram of the contact-element modeling method.

2.2.2. Contact Relation

Compared to the cohesive unit, the contact relation is more convenient for simulating the interface cohesive displacement characteristics of bolt and concrete. Specific operations are carried out in modules that interact with components, such as assigning values to the attributes of interactions and setting interaction areas. The process of defining it follows this path: Interaction → Property → Create → Mechanical → Cohesive Behavior → Damage → Criterion. Among them, key parameters such as friction coefficient, bond stiffness coefficient, and initial stress value require relevant specifications and test verification for accurate simulation.

3. Laboratory Test

3.1. Experiment Objective and Method

Anchoring length is an important index affecting the anchoring performance of a bolt, and its value dramatically impacts the bolt's safety. In this study, the influence of anchoring length on bolt anchoring performance was studied by performing full-scale destructive laboratory tests on bolts with different anchoring lengths. Moreover, the results were used in the numerical simulation to verify the model's reliability.

A single bolt was utilized as a group during the horizontal pull test. A bolt was also used to connect two concrete blocks in series, and two perforated hydraulic jack sets were arranged horizontally on both sides to ensure the bolt's horizontal stress. The bolt stress and the relative displacement between the bolt and concrete were recorded during the test using a displacement meter and a dynamometer. This loading device does not require jigging, which helps avoid test errors caused by the poor shear performance of the GFRP anchor rod. The horizontal load was applied synchronously through two through-core jack groups. Additionally, parallel experiments were completed by applying one load and obtaining two test data sets.

Two types of concrete blocks with 800 × 800 × 500 mm and 800 × 800 × 900 mm sizes were used to test the GFRP anchors with different anchoring lengths. The test device is shown in Figure 2 (an 800 × 800 × 500 mm solid anchor size was taken as an example).

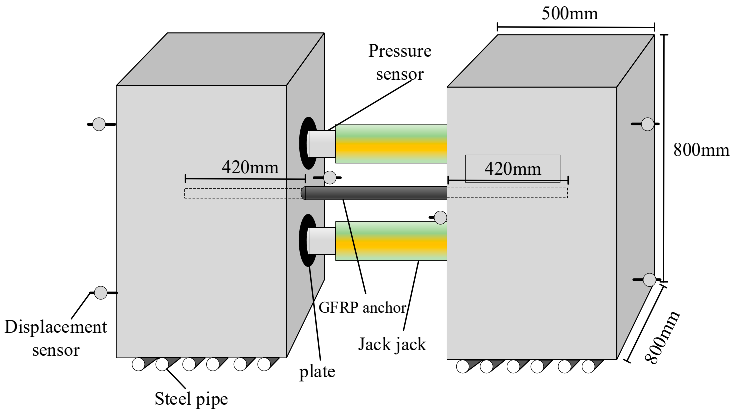

Figure 2. Schematic diagram of the test device.

3.2. Test Materials

3.2.1. GFRP Anchor

Epoxy GFRP anchors were used in the test and were composed with about 25% epoxy and 75% glass fiber. The diameter of the bolt was 28 mm, the measured density was 2.1 g/cm^3, the ultimate shear strength was 150 MPa, and the elastic modulus was 51 GPa. The anchoring lengths of the GFRP bolt were 420 mm (15D) and 840 mm (30D), where D is the bolt diameter.

3.2.2. Concrete Block

Plain concrete with a C25 strength grade was used in concrete blocks with an 800 mm × 800 mm section and 500 mm and 900 mm thicknesses. The concrete block was supported using a wood mold. The wood mold's bottom was separated from the ground by equally spaced seamless steel pipes to prevent uneven force caused by excessive friction in the concrete block during the test process, eliminating its effects on the test results. In order to measure the concrete's mechanical index, three groups of standard test blocks were made under the same conditions. The specific test material parameters are shown in Table 1.

Table 1. Test material parameters.

Test Number	Bolt Diameter (mm)	Anchorage Length (mm)	Bolt Elastic Modulus (GPa)	Concrete Strength Class	Concrete Block Size (mm^3)
S420	28	420	150	C25	800 × 800 × 500
S840	28	840	150	C25	800 × 800 × 900

3.3. Test Process

Before concrete pouring, the anchor bar was installed in the wooden mold to prevent bolt deflection during concrete casting, ensuring the accuracy of the bolt's applied horizontal stress. When concrete is poured, it typically requires vibrations to ensure the compactness of the anchorage area. Here, the time of each vibration was 20 to 30 s. After 28 days of curing, the compressive strength of the standard concrete test block reached 25.4 MPa, which met the strength requirements.

The test was started after calibrating the displacement meter and dynamometer. Step-by-step loading was adopted in the test. Each stage load was 40 kN, and the load was uniformly applied at a 0.2 kN/s rate until the test bolt was damaged. The relative slip between the GFRP anchor bolt and the concrete block was recorded immediately after applying each grade load. The test process strictly followed the requirements of the *Technical specification for anti-floating anchors* (YB/T4659-2018) [31]. The specific test process is shown in Figure 3, and the test results are depicted.

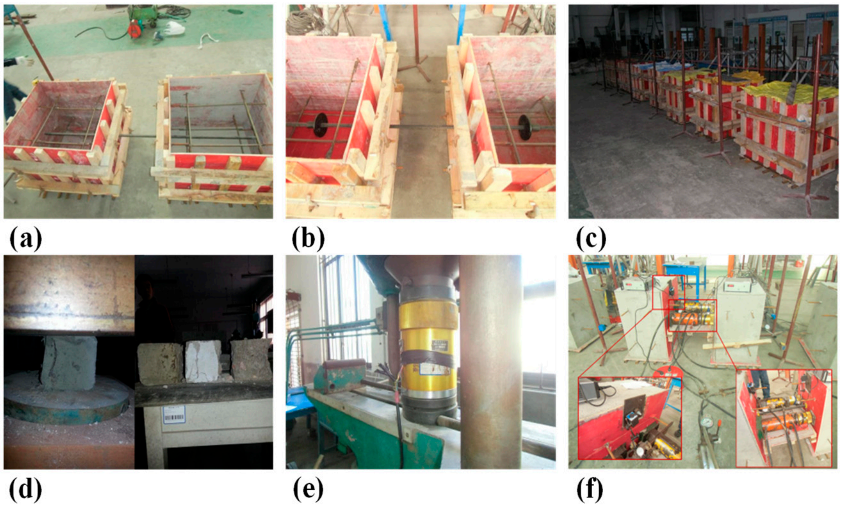

Figure 3. Laboratory test photos: (**a**) mold-making, (**b**) bolt installation, (**c**) concrete pouring and curing, (**d**) concrete strength test, (**e**) calibration of load sensor, (**f**) test load.

4. GFRP Anchoring Numerical Simulation

4.1. Constitutive Model

4.1.1. Concrete Constitutive Model

Concrete is an elastic–plastic cementitious material that undergoes various cracking degrees when subjected to stress. Generally, three models simulate concrete behavior in ABAQUS: the concrete damage-plasticity model, the concrete smeared-cracking model, and the concrete brittle-cracking model. In this paper, the concrete damage-plasticity model was selected. The concrete damage model parameters were obtained according to the specifications of the *Code for design of concrete structures* (GB 50010-2010) [32], from which, the stress–strain relationship is shown in Figure 4.

The stress–strain values of concrete under tension and compression were obtained by conducting tensile and compression tests according to the concrete specifications. The concrete damage parameters were calculated using the equations that follow.

When concrete is compressed:

$$\sigma = (1 - d_c) E_c \varepsilon \tag{1}$$

$$\text{When } x \leq 1,\ d_c = 1 - \frac{\rho_c n}{n - 1 + x^n}$$

$$\text{When } x > 1,\ d_c = 1 - \frac{\rho_c}{\alpha_c (x-1)^2 + x}$$

$$\rho_c = \frac{f_c}{E_c \varepsilon_c} \tag{2}$$

$$n = \frac{E_c \varepsilon_c}{E_c \varepsilon_c - f_c} \tag{3}$$

$$x = \frac{\varepsilon}{\varepsilon_c} \tag{4}$$

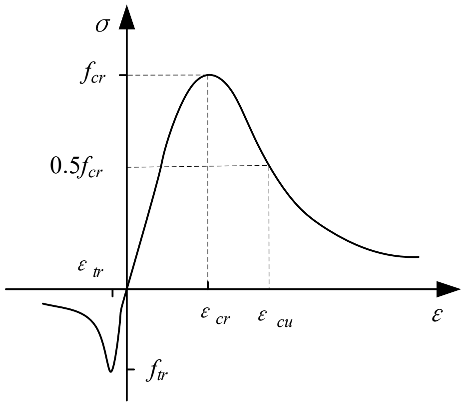

Figure 4. Concrete constitutive model, where f_{cr} and f_{tr} are the concrete uniaxial compressive and tensile strength, respectively, and ε is the strain value of concrete corresponding to strength.

When concrete is tensioned:

$$\sigma = (1-d_t)E_c\varepsilon \tag{5}$$

$$\text{When } x \leq 1,\ d_c = 1-\rho_t(1.2 - 0.2x^5)$$

$$\text{When } x > 1,\ d_t = 1-\frac{\rho_t}{\alpha_t(x-1)^{1.7} + x}$$

$$\rho_t = \frac{f_t}{E_c \varepsilon_t} \tag{6}$$

$$x = \frac{\varepsilon}{\varepsilon_t} \tag{7}$$

where σ_c and σ_t are the compressive and tensile stresses of concrete, f_c and f_t are the compressive and tensile strength of concrete, respectively, ε_c and ε_t are the peak compressive and tensile strain values of concrete, respectively, and d_c and d_t are the evolution parameters of the concrete damage under compression and tension, respectively.

Typically, when the concrete damage model is utilized, its evolution law is derived according to the energy equivalence model and the strain equivalence model, and its damage parameters can be obtained using the following equations:

$$E_0(1-d) = E_0(1-D)^2 \tag{8}$$

$$D = 1-\sqrt{1-d} \tag{9}$$

$$d = 1-\sqrt{\frac{\sigma}{E \cdot \varepsilon}} \tag{10}$$

where D is the plastic damage factor of concrete, and d is the damage evolution parameter.

4.1.2. GFRP Anchor Constitutive Model

GFRP bolts consist of glass fiber and epoxy resin with anisotropic material properties. As shown in Figure 5, the stress–strain relationship under the standard state presents a linear distribution, and there is no obvious yield stage compared to reinforced bolts.

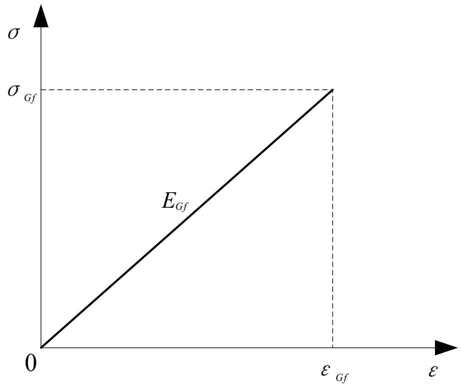

Figure 5. Constitutive model of GFRP anchor, where E_{Gf} is the elastic modulus of GFRP, and σ_{Gf} and ε_{Gf} are the ultimate stress value and ultimate strain value of GFRP, respectively.

4.1.3. Interfacial Relation Constitutive Model

The cohesive bond relationship between the GFRP bolt and the concrete interface was defined using the cohesive model. Before and after damage are represented by ascending and descending segments, respectively. The cohesive element constitutive model is shown in Figure 6, where slope K is the penalty stiffness of the cohesive element, and the curve's envelope area is the fracture damage energy.

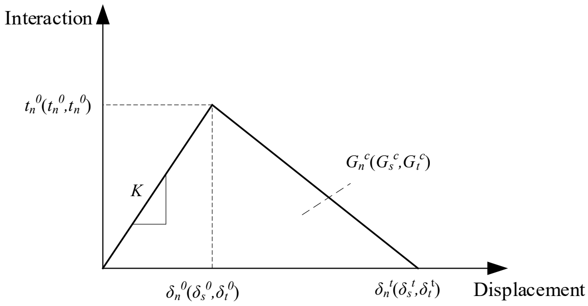

Figure 6. Cohesive model constitutive equation.

The main interface parameters include stiffness coefficient, maximum nominal stress, normal and shear fracture energy, and viscosity coefficient. The maximum nominal stress criterion of the Maxs Damage was used to represent the degradation of interface elements when the initial critical damage was defined. Accordingly, interface damage began to occur when the maximum nominal strain ratio reached 1. Its expression is shown in Equation (11).

$$\max\left\{\frac{\langle t_n \rangle}{t_n^0}, \frac{t_s}{t_s^0}, \frac{t_t}{t_t^0}\right\} = 1 \tag{11}$$

where $t_n{}^0$, $t_s{}^0$, and $t_t{}^0$ represent the peak nominal normal stress of the cohesive element in the normal direction and x and y tangential directions, respectively. Macaulay brackets indicate that simple normal stresses or normal displacements do not cause damage.

In this study, the Benzeggagh–Kenane Law (BK criterion) was used to represent the evolution law of damage when the interface relationship reached the failure criterion. The BK criterion is defined in Equation (12).

$$G_n^c + \left(G_s^c - G_n^c\right)\left(\frac{G_S}{G_T}\right)^{\eta} = G^c \tag{12}$$

where $G^c = G_n + G_s + G_t$, $G_S = G_s + G_t$, $G_T = G_S + G_t$ and G_n, G_s, G_t are the interface fracture failure energy in the corresponding failure direction, $G_n{}^c$, $G_s{}^c$, $G_t{}^c$ is the critical fracture failure energy in the corresponding failure direction, and η is the material parameter.

4.2. Establishing the Model

4.2.1. Modeling

This numerical simulation is based on full-scale laboratory test conditions and adopts the laboratory test and numerical model in equal proportions for modeling. The model adopted an axisymmetric simulation method, and the concrete block and GFRP bolt were separately defined. The concrete plane size was 400 × 500 mm and 400 × 900 mm. The surface of the GFRP bolt used a form of ring thread. The thread size was taken to be the same as that of the test bolt, and its specific parameters are shown in Table 2. Once the component was created, the material properties of the GFRP anchor bolt and concrete slab were defined. GFRP bolt was assumed to be an isotropic elastic–plastic material, and its density, elasticity, and plasticity parameters were defined accordingly. The plastic parameters were taken as the stress–strain values in the laboratory single-bar pulling test. A concrete plastic-damage model was adopted for concrete slabs, and its parameters were stress–strain values collected from the standard tensile and compressive tests of the C25 concrete. The damage parameters were calculated according to the expressions in the specifications. Once the assignment of component material attributes was completed, each component was assembled. The axisymmetric model of the concrete block anchored using the GFRP anchor bolt after assembly is shown in Figure 7.

Table 2. Test bolt shape parameters.

Bolt Diameter (mm)	Outer Diameter (mm)	Inner Diameter (mm)	Thread Pitch (mm)	Tooth Width (mm)	Tooth Height (mm)
28	28	25.7	10	2	1.15

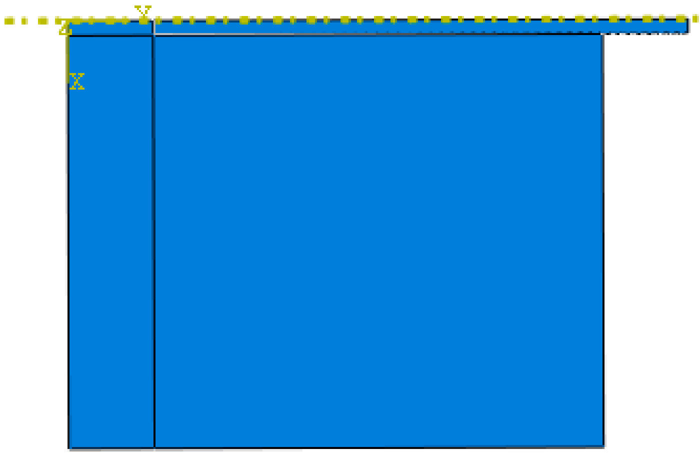

Figure 7. Axisymmetric model of GFRP anchorage concrete bottom plate.

4.2.2. Determination of Contact Relations and Boundary Conditions

This section describes cohesive-element contact relations and interface friction based on the interface selection between the bolt and concrete block. When setting interface friction parameters, the default penalty function contact was adopted, where the tangential friction coefficient was taken as 0.3. The cohesive element utilized a tractor-separation criterion, which specifies the stiffness coefficient. The damage criterion adopted the initial maximum nominal stress, and the damage evolution used the BK energy criterion and the linear softening method. Given that the stiffness of the GFRP bolt is greater than that of concrete and that this study focused on the bonding property between the GFRP bolt and concrete, the bolt's outer surface was chosen as the main surface, and the concrete interface in contact with GFRP bolt was defined as the slave surface. In order to completely simulate the laboratory test conditions, the displacement boundary conditions were applied to the concrete's end face, and the pressure load was applied to the GFRP anchor's upper surface to simulate the pulling load of the anchor.

4.2.3. Grid Division and Solving Settings

Figure 8 shows the grid division. In order to improve the calculation accuracy, CAX4R grid elements were implemented in the concrete blocks and GFRP anchors, and the reduction integral algorithm and hourglass control method were adopted. Step-by-step activation of the geometric nonlinearity and automatic stabilization with 10,000 steps and 0.001 minimum increment were used to enhance the convergence.

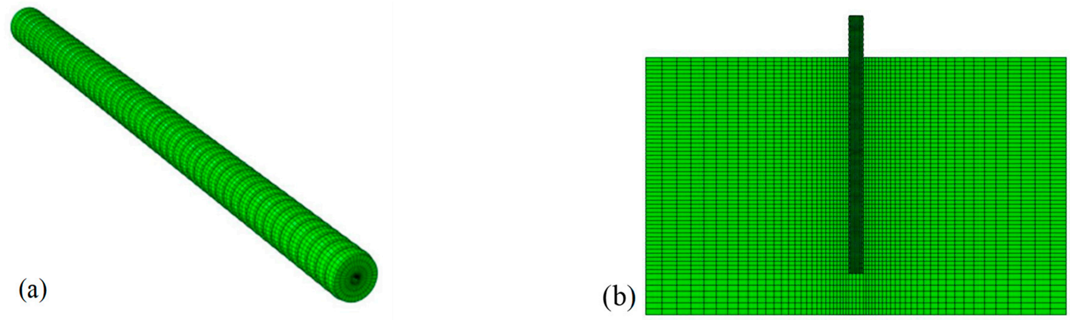

Figure 8. Network division of GFRP anchorage model: (**a**) GFPR anchor bolt, (**b**) anchorage system.

5. Calculation Results and Model Verification

5.1. Numerical Simulation Results and Analysis

The difficulty of this numerical simulation lies in the contact relation setting because the bolt's surface is rough, and the bonding–displacement relation between the interface must be derived from the specification and test. The anchoring performance of GFRP bolts with a 28 mm diameter and 420 and 840 mm anchoring lengths was simulated. A three-dimensional solid view was built by 90° sweeping. The displacement unit was mm, the load unit was kN, and the stress unit was MPa.

5.1.1. Anchor L420 Simulation Results

Under the simulated pulling load at the rod end, the displacement of the GFRP bolt with an anchorage length of 420 mm along the rod end's axis direction increased as the load rose. When the load reached 240 kN, the bolt had a large displacement, the simulated displacement did not converge, and the operation terminated. The analysis reveals that the bolt was pulled out and damaged. Figure 9 indicates that the maximum displacement of the top bolt before failure was 10.27 mm. Due to the linear elastic behavior of the GFRP bolt, an elastic–plastic slip was observed along the axial direction of the bolt, and the step type varied as the buried depth increased.

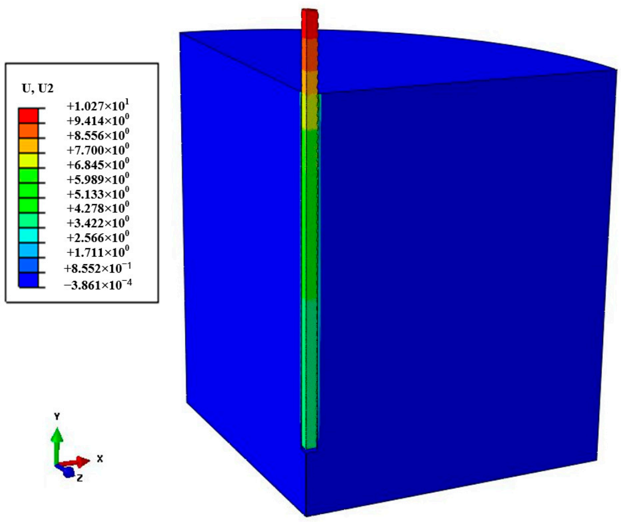

Figure 9. L420 model failure diagram.

5.1.2. Anchor L840 Simulation Results

For the GFRP bolt with an anchorage length of 420 mm, under the simulated pulling load at the rod end, the bolt displacement in the rod end's axis direction rose as the load increased. Figure 10 indicates that when the load reached 380 kN, the displacement of the bolt end increased rapidly to 30.37 mm. The bolt body appeared to have shrunk at the anchor hole, and it broke. Due to the fracture of the bar body, the stress decreased, and the position of the bar body moved back and shrunk.

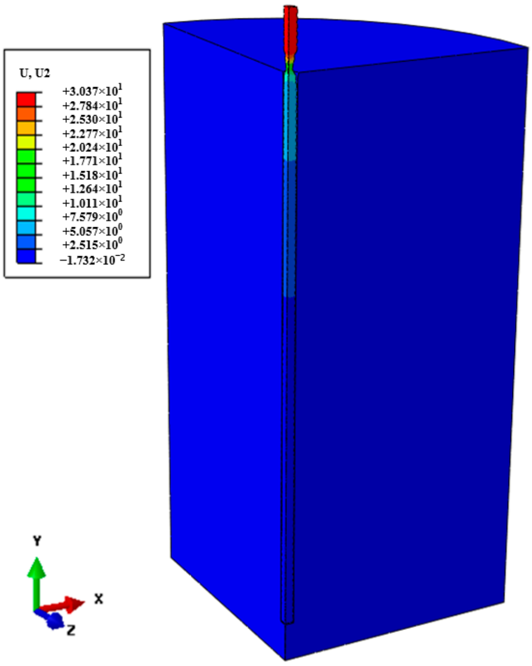

Figure 10. L840 model failure diagram.

Through the simulation of GFRP anchors with anchoring lengths of 420 mm and 840 mm, it can be seen from the numerical analysis results that our interface relationship model is viable for the numerical simulation of GFRP anchors and foundation plate anchoring.

5.2. Contrastive Analysis of Load–Displacement Curve

Figure 11 depicts the load–displacement curves of GFRP bolts with various anchoring lengths under different pulling loads. The axial node of the rod inside the anchor hole was selected as the displacement and stress output of the GFRP bolt from the numerical simulation to reduce the influence of the exposed bolt on the displacement results. It can be seen from Figure 11a that test-measured values and numerical-simulation-calculated values were highly coincidental. The GFRP bolt with an anchoring length of 420 mm was pulled out and damaged, the bolt body and concrete unstick, load reduction, and displacement rapidly increased, and the figure's curve had a descending section. Figure 11b reveals that the bolt displacement increased uniformly with the load during the early loading phase. In the final loading stage, the bolt reached its ultimate strength and accelerated the displacement until damaged.

Figure 11 illustrates that the load peak value of the numerical simulation was higher than the test value, but the measured displacement of the bolt was slightly greater than the simulation's calculated value during the early loading stage. The reasons were as follows: first, the interface bonding between the test bolt and concrete was not uniform enough during the laboratory test; second, there were inevitable errors in reading test data manually.

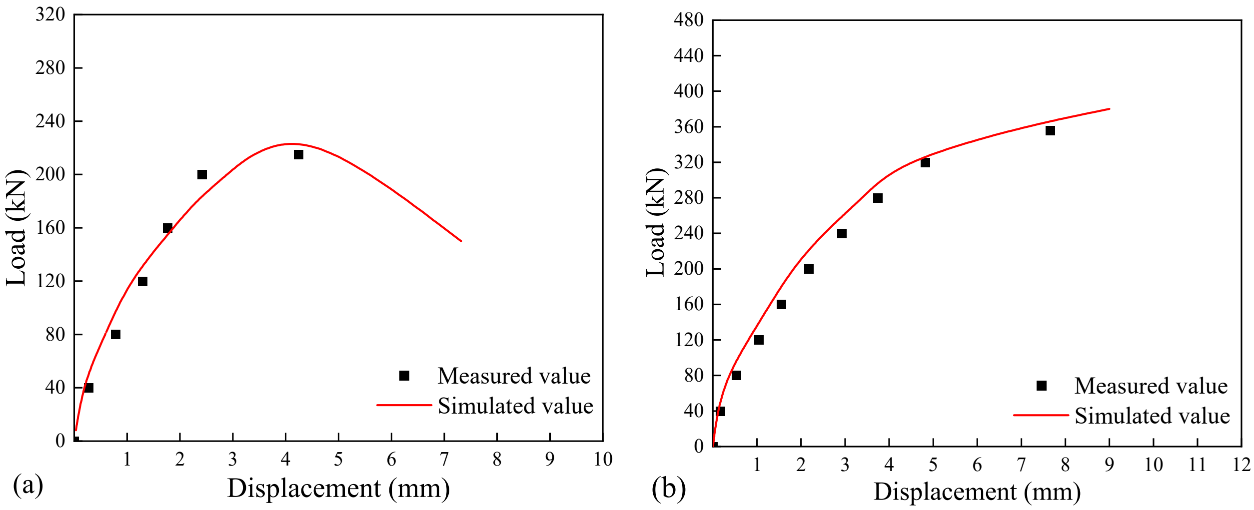

Figure 11. GFRP bolt load–displacement curves: (**a**) anchor L420, (**b**) anchor L840.

5.3. Different Load Levels of Stress Distribution

5.3.1. Anchor L420

Figure 12 depicts the stress nephogram of the GFRP anchor under different loads. The stress nephogram corresponding to the bolt was determined before, during, and after the drawing process, where the respective loads were 40, 80, 160, and 240 kN. Figure 12 demonstrates that the bolt's axial stress was successfully transferred from the loading end to the anchoring depth under the load. When the bolt displacement occurred, the stress concentration happened near the bolt hole, as shown in Figure 12d. Along with the load increase, the interface bonding stress decreased continuously, and the bolt finally appeared to have a large displacement and became unbonded with the concrete block.

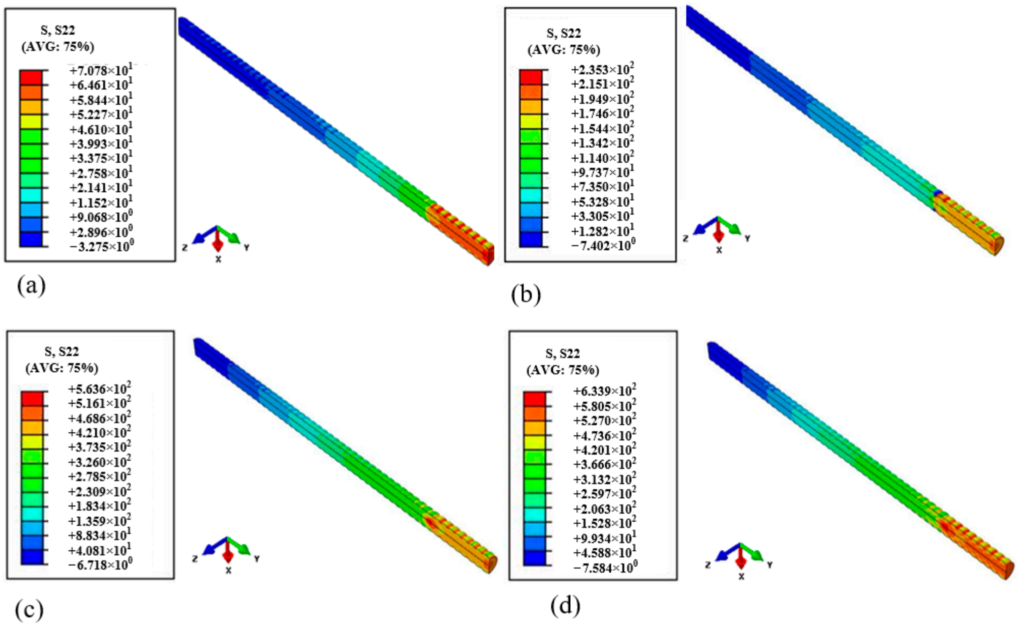

Figure 12. Stress nephogram of GFRP bolt with anchor length of 420 mm: (**a**) *F* = 40 kN, (**b**) *F* = 80 kN, (**c**) F = 160 kN, (**d**) F = 240 kN.

5.3.2. Anchor L840

Figure 13 depicts the stress nephogram of the GFRP bolt with a load of 40, 120, and 240 kN after failure. Figure 13a,b indicate that the stress nephograms of bolts L420 and L840 under pulling load were similar in the early stages of bolt loading. When the maximum stress in the stress cloud diagram reached the ultimate tensile strength of the bolt (702 MPa), the anchor reached the stress peak near the anchor hole, the apparent tearing failure occurred, and the bolt was pulled out. During this time, the stress of the bolt body in the anchorage section rapidly decreased.

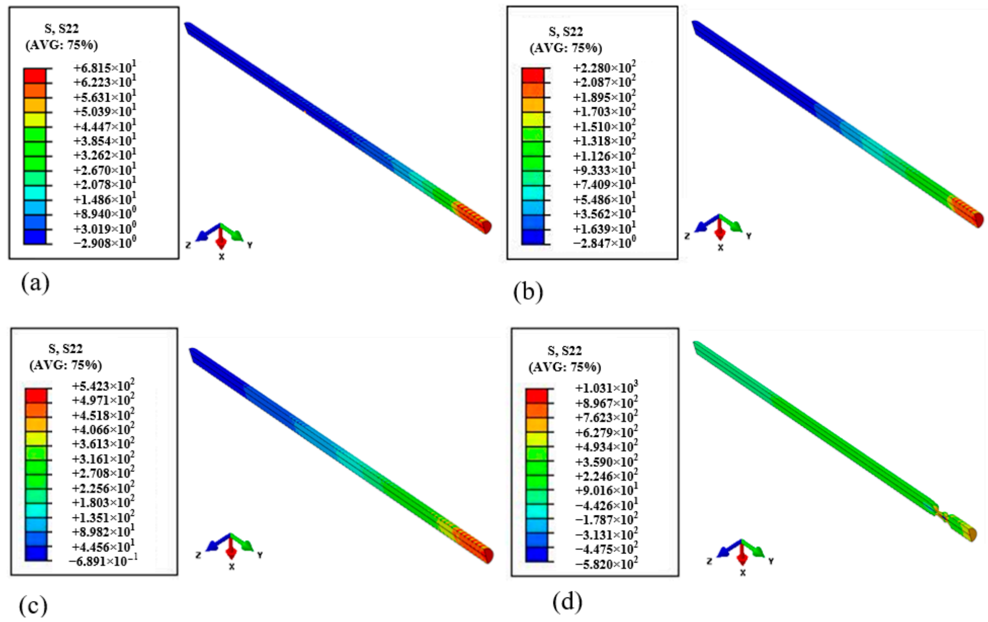

Figure 13. Stress nephogram of GFRP bolt with anchor length of 840 mm: (**a**) F = 40 kN, (**b**) F = 120 kN, (**c**) F = 240 kN, (**d**) after bolt pull-out.

6. Simulation of GFRP Bolts at Different Anchoring Lengths

6.1. Anchor Axial Stress Distribution Law

Based on the above model parameters, the relationships between concrete, bolt, and interface remained unchanged, while the anchorage length of the GFRP anchor was modified. The stress of the GFRP anchor with anchorage lengths of 18D, 21D, 24D, 30D, and 33D was simulated under the pull load.

We investigated the distribution law of axial force of GFRP bolt under varying loads; Figure 14 demonstrates how identically spaced integral elements were selected along the anchoring depth to determine the axial stress values of integral elements under various loads. We discovered that the axial stress of the GFRP bolt was at its maximum at the anchor hole, tended to zero at the end of the bolt, and decreased as the anchoring length increased. This showed that under the influence of a load, the load was successively transferred along the direction of the anchoring depth by axial force, and with the increase of anchoring length, the interface bond stress between bolt and concrete increased as the load rose.

When comparing the axial stress distribution of GFRP anchors with different anchoring lengths, the axial stress transfer depth was identical under the same load. The bolt axial stress change rate decreased gradually along the direction of anchoring depth, and this phenomenon became more evident as the anchoring length rose. This indicates that as the distance to the anchor hole decreased, the load borne by the GFRP bolt body increased. In contrast, the farther that the bolt was from the anchor hole, the smaller the load-sharing proportion was. This demonstrates that the area near the anchor hole was the weakest and would fail first, which was consistent with the failure pattern of the bolt when it was pulled out in the laboratory test. As shown in Figure 14f,g, when the anchoring length exceeded 840 mm, the load was no longer be transferred to the depth, indicating that the critical anchoring length of the bolt was reached.

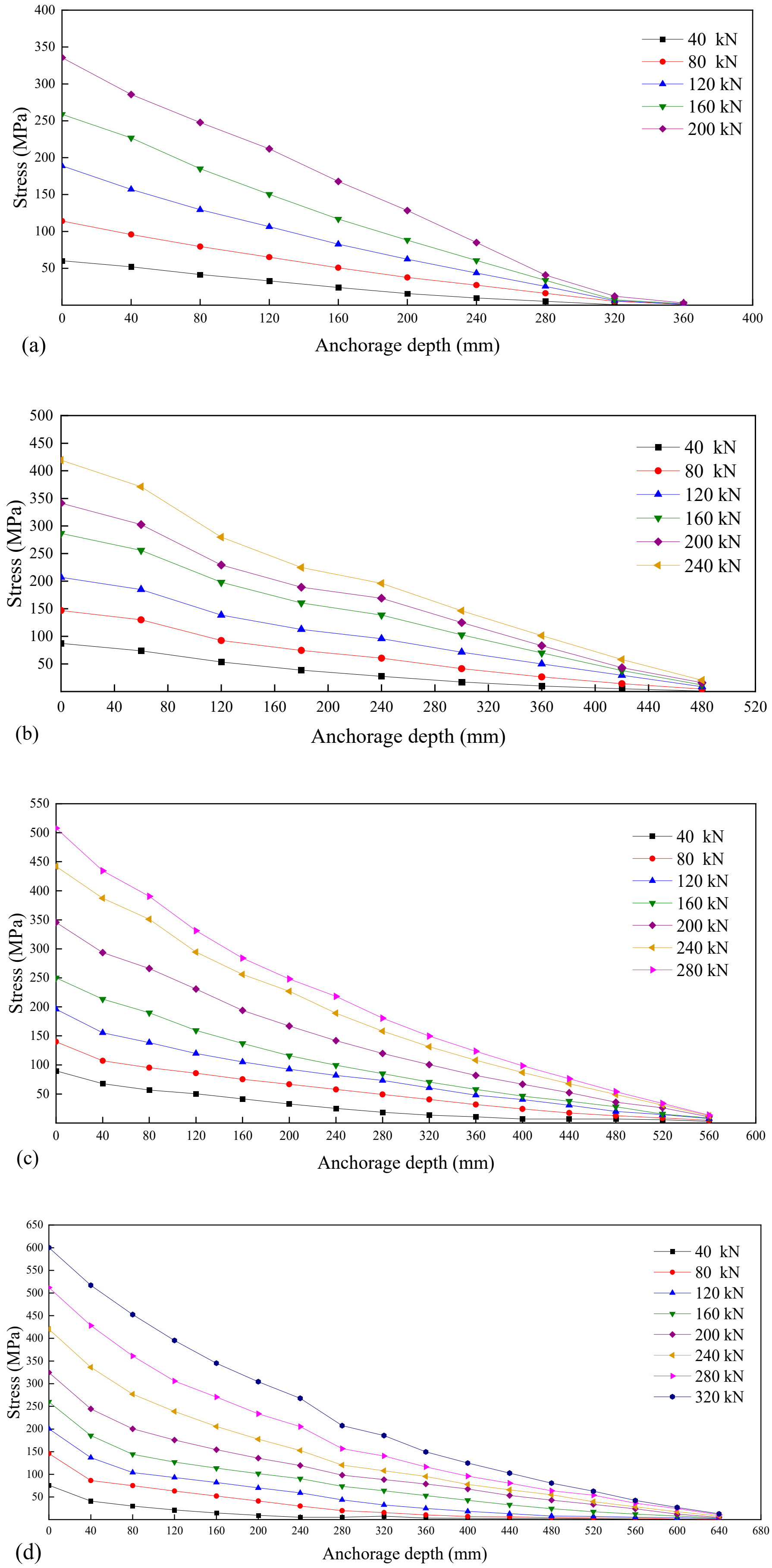

Figure 14. *Cont*.

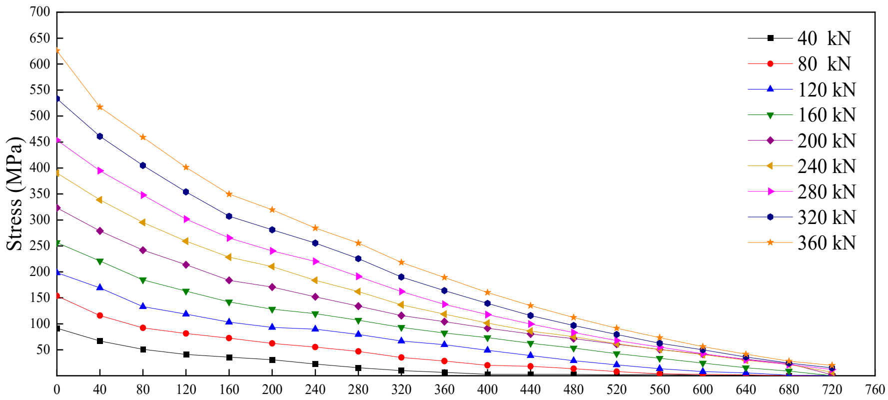

(e)

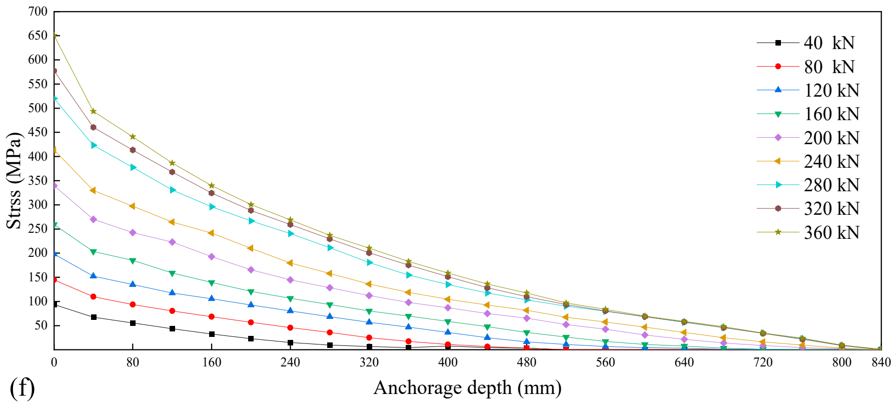

(f)

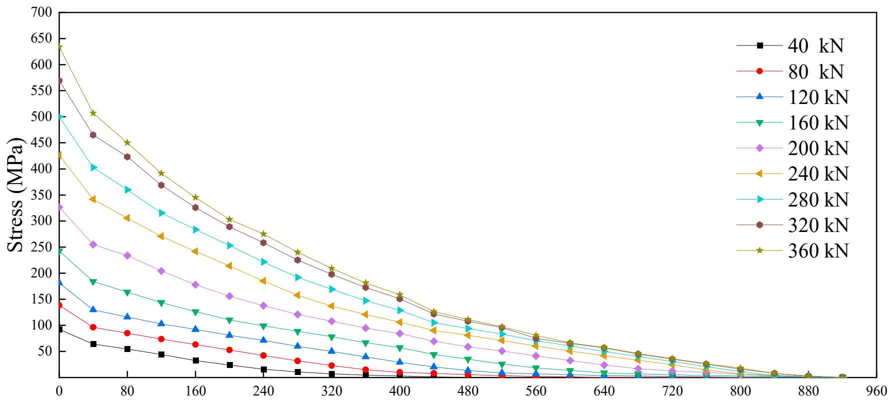

(g)

Figure 14. Variation law of bolt axial stress with anchoring depth: (**a**) 15*D*/420 mm, (**b**) 18*D*/504 mm, (**c**) 21*D*/588 mm, (**d**) 24*D*/672 mm, (**e**) 27*D*/756 mm, (**f**) 30*D*/840 mm, (**g**) 33*D*/924 mm.

6.2. Bolt Load–Displacement Curve

Figure 15 depicts the GFRP bolt load–displacement relationship. The peak load before the bolt failed was selected as the bolt's final load. The bolt load–displacement curve with various anchoring lengths had the same trend. As the load developed, the change of bolt position was gradually accelerated. Under the same load level, the bolt displacement reduced as the anchorage length increased, and the final displacement rose as the anchorage length increased. The load–displacement curves of GFRP anchors with anchoring lengths of 27D, 30D, and 33D were nearly identical, indicating that when the anchoring length exceeded 27D, simply increasing the anchoring length cannot effectively improve the external anchoring strength of GFRP anchors.

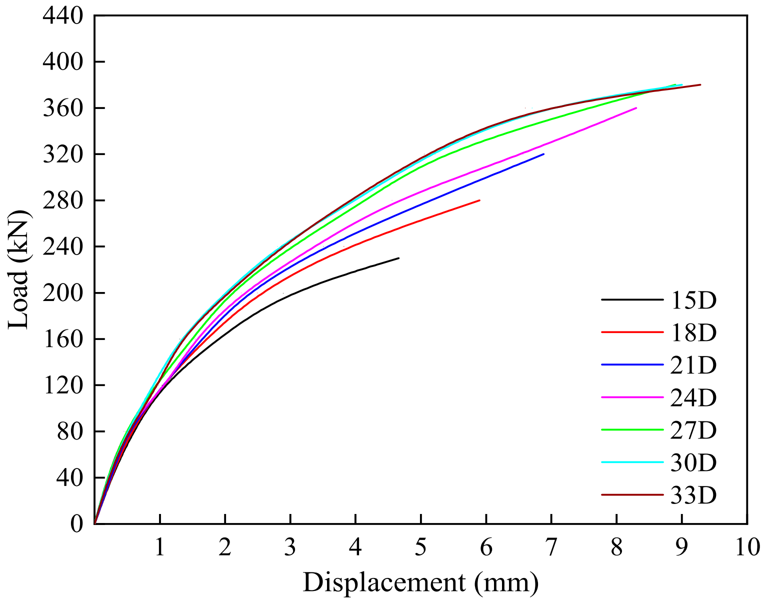

Figure 15. Bolt load–displacement curve.

7. Conclusions

1. Our calculation model of axial symmetry between the GFRP anchor rod and concrete, cohesive elements can effectively simulate the bonding relationship between GFRP anchor and concrete.
2. ABAQUS software was applied to develop a fine model of the laboratory test anchorage system, and a simulation of the anti-floating anchor L420 and L840 was performed. The load–displacement curves derived from simulation and laboratory tests were in good agreement, and the stress distribution nephogram obtained from the simulation better described the load-transfer law of the bolt. At the same time, the reliability of ABAQUS software for analyzing the anchoring performance of the GFRP bolt was verified, as well as the rationality and scientificity of parameter selection.
3. A numerical analysis of the anchoring performance of GFRP anchors with different anchoring lengths indicated that the axial stress transfer depth was identical under the same load. Under increasing bolt anchorage length, the attenuation rate of bolt axial stress gradually rose. The anchor bolt near the anchor hole is a weak area and will be the first to break. When the anchoring length exceeded 27D, the external anchoring strength of the GFRP bolt could not be effectively improved by increasing the anchoring length. This simulation offers a novel approach for studying the anchorage performance of GFPR anchor bolts and concrete.

Author Contributions: Writing—original draft: G.S.; Formal analysis: X.B.; Writing—review & editing: S.S.; Investigation: L.Z.; Writing—review & editing: J.Y. and D.J.; Data curation: M.Z.; Conctueptualization: N.Y. All authors have read and agreed to the published version of the manuscript.

Funding: This research was supported by the National Natural Science Foundation of China (Grant no. 51708316), the Key Program of Natural Science Foundation of Shandong Province (Grant No. ZR2020KE009), the China Postdoctoral Science Foundation Funding (2018M632641), Shandong Provincial Post-doctoral Innovation Project (Grant No. 201903043).

Data Availability Statement: The data presented in this study are available upon request from the corresponding author.

Conflicts of Interest: The authors declare no conflict of interest.

References

1. Kuang, Z.; Zhang, M.; Bai, X. Load-bearing characteristics of fibreglass uplift anchors in weathered rock. *Proc. Inst. Civ. Eng.-Geotech. Eng.* **2020**, *173*, 49–57. [CrossRef]
2. Bai, X.; Liu, X.; Zhang, M.; Wang, Y.; Kuang, Z.; Yan, N. Stress transfer properties and displacement difference of GFRP antifloating anchor. *Adv. Civ. Eng.* **2020**, *2020*, 8894720. [CrossRef]
3. Karataş, M.A.; Gökkaya, H. A review on machinability of carbon fiber reinforced polymer (CFRP) and glass fiber reinforced polymer (GFRP) composite materials. *Def. Technol.* **2018**, *14*, 318–326. [CrossRef]
4. D'Antino, T.; Pisani, M.A.; Poggi, C. Effect of the environment on the performance of GFRP reinforcing bars. *Compos. Part B Eng.* **2018**, *141*, 123–136. [CrossRef]
5. Frenelus, W.; Peng, H.; Zhang, J. An insight from rock bolts and potential factors influencing their durability and the long-term stability of deep rock tunnels. *Sustainability* **2022**, *14*, 10943. [CrossRef]
6. Yuan, B.; Li, Z.; Chen, W.; Luo, Q.; Yang, G.; Wang, Y. Experimental study on lateral cyclic loading model of pile-soil system based on PIV technique and fractal theory. *Chin. J. Rock Mech. Eng.* **2022**, 1–17. [CrossRef]
7. Smet, J.; Huybrechts, N.; Van Lysebetten, G.; Verstraelen, J.; François, S. Optical fiber strain measurements and numerical modeling of load tests on grouted anchors. *J. Geotech. Geoenviron. Eng.* **2019**, *145*, 04019103. [CrossRef]
8. Karimi, M.R.; Abrinia, K.; Hamdia, K.M.; Hashemianzadeh, S.M.; Baniassadi, M. Effects of functional group type and coverage on the interfacial strength and load transfer of graphene-polyethylene nanocomposites: A molecular dynamics simulation. *Appl. Phys. A* **2022**, *128*, 341. [CrossRef]
9. Soong, W.H.; Raghavan, J.; Rizkalla, S.H. Fundamental mechanisms of bonding of glass fiber reinforced polymer reinforcement to concrete. *Constr. Build. Mater.* **2011**, *25*, 2813–2821. [CrossRef]
10. Kou, H.L.; Li, W.; Zhang, W.C.; Zhou, Y.; Zhou, X.L. Stress monitoring on GFRP anchors based on fiber Bragg grating sensors. *Sensors* **2019**, *19*, 1507. [CrossRef]
11. Lu, W.; Zhao, D.; Mao, X.F.; Ai, Y. Experimental study on bond-slip behavior of bamboo bolt-modified slurry interface under pull-out load. *Adv. Civ. Eng.* **2018**, *2018*, 6960285. [CrossRef]
12. Ceroni, F.; Darban, H.; Luciano, R. Analysis of bond behavior of injected anchors in masonry elements by means of Finite Element Modeling. *Compos. Struct.* **2020**, *241*, 112099. [CrossRef]
13. Lee, J.Y.; Kim, T.Y.; Kim, T.J.; Yi, C.K.; Park, J.S.; You, Y.C.; Park, Y.H. Interfacial bond strength of glass fiber reinforced polymer bars in high-strength concrete. *Compos. Part B Eng.* **2020**, *183*, 107602. [CrossRef]
14. Carozzi, F.G.; Colombi, P.; Fava, G.; Poggi, C. Mechanical and bond properties of FRP anchor spikes in concrete and masonry blocks. *Compos. Struct.* **2018**, *183*, 185–198. [CrossRef]
15. Tighiouart, B.; Benmokrane, B.; Gao, D. Investigation of bond in concrete member with fibre reinforced polymer (FRP) bars. *Constr. Build. Mater.* **1998**, *12*, 453–462. [CrossRef]
16. Mazaheripour, H.B.J.A.O.; Barros, J.A.; Sena-Cruz, J.M.; Pepe, M.; Martinelli, E. Experimental study on bond performance of GFRP bars in self-compacting steel fiber reinforced concrete. *Compos. Struct.* **2013**, *95*, 202–212. [CrossRef]
17. Tekle, B.H.; Khennane, A.; Kayali, O. Bond properties of sand-coated GFRP bars with fly ash–based geopolymer concrete. *J. Compos. Constr* **2016**, *20*, 04016025. [CrossRef]
18. Li, T.; Zhu, H.; Wang, Q.; Li, J.; Wu, T. Experimental study on the enhancement of additional ribs to the bond performance of FRP bars in concrete. *Constr. Build. Mater.* **2018**, *185*, 545–554. [CrossRef]
19. Zhang, B.; Zhu, H.; Wu, G.; Wang, Q.; Li, T. Improvement of bond performance between concrete and CFRP bars with optimized additional aluminum ribs anchorage. *Constr. Build. Mater.* **2020**, *241*, 118012. [CrossRef]
20. Rolland, A.; Quiertant, M.; Khadour, A.; Chataigner, S.; Benzarti, K.; Argoul, P. Experimental investigations on the bond behavior between concrete and FRP reinforcing bars. *Constr. Build. Mater.* **2018**, *173*, 136–148. [CrossRef]
21. Hu, Z.; Shah, Y.I.; Yao, P. Experimental and numerical study on interface bond strength and anchorage performance of steel bars within prefabricated concrete. *Materials* **2021**, *14*, 3713. [CrossRef]
22. Yokota, Y.; Zhao, Z.; Nie, W.; Date, K.; Iwano, K.; Okada, Y. Experimental and numerical study on the interface behaviour between the rock bolt and bond material. *Rock Mech. Rock Eng.* **2019**, *52*, 869–879. [CrossRef]
23. Alhassan, M.A.; Al-Rousan, R.Z.; Taha, H.M. Precise finite element modelling of the bond-slip contact behavior between CFRP composites and concrete. *Constr. Build. Mater.* **2020**, *240*, 117943. [CrossRef]
24. Veljkovic, A.; Carvelli, V.; Haffke, M.M.; Pahn, M. Concrete cover effect on the bond of GFRP bar and concrete under static loading. *Compos. Part B Eng.* **2017**, *124*, 40–53. [CrossRef]
25. Wei, M.W.; Xie, J.H.; Zhang, H.; Li, J.L. Bond-slip behaviors of BFRP-to-concrete interfaces exposed to wet/dry cycles in chloride environment. *Compos. Struct.* **2019**, *219*, 185–193. [CrossRef]
26. Fang, Z.; Fang, C.; Jiang, Z.; Wang, Z.; Li, J.; Zhang, Y. Mechanical properties of CFRP bar and bond-type anchorage system after elevated temperature exposure. *Acta Mater. Compos. Sin.* **2021**, *38*, 4031–4041.
27. Gooranorimi, O.; Suaris, W.; Nanni, A. A model for the bond-slip of a GFRP bar in concrete. *Eng. Struct.* **2017**, *146*, 34–42. [CrossRef]
28. Yoo, D.Y.; Kwon, K.Y.; Park, J.J.; Yoon, Y. Local bond-slip response of GFRP rebar in ultra-high-performance fiber-reinforced concrete. *Compos. Struct.* **2015**, *120*, 53–64. [CrossRef]

29. Tekle, B.H.; Khennane, A.; Kayali, O. Bond behaviour of GFRP reinforcement in alkali activated cement concrete. *Constr. Build. Mater.* **2017**, *154*, 972–982. [CrossRef]
30. Rezazadeh, M.; Carvelli, V.; Veljkovic, A. Modelling bond of GFRP rebar and concrete. *Constr. Build. Mater.* **2017**, *153*, 102–116. [CrossRef]
31. *YB/T4659-2018*; Technical Specification for Anti-Floating Anchors. Metallurgical Industry Press: Beijing, China, 2018.
32. *GB 50010-2010*; Code for Design of Concrete Structures. China Architecture & Building Press: Beijing, China, 2010.